

## Novel High-Speed Polarization Source For Decoy-State BB84 Quantum Key Distribution Over Free Space and Satellite Links

Zhizhong Yan,<sup>1, a)</sup> Evan Meyer-Scott,<sup>1</sup> Jean-Philippe Bourgoin,<sup>1</sup> Brendon L Higgins,<sup>1</sup> Nikolay Gigov,<sup>1</sup> Allison MacDonald,<sup>1, 2</sup> Hannes Hübel,<sup>1, 3</sup> and Thomas Jennewein<sup>1, b)</sup>

<sup>1)</sup>*Institute for Quantum Computing, University of Waterloo,  
200 University Avenue W, Waterloo N2L 3G1, Canada*

<sup>2)</sup>*Physics Department, University of Alberta, Edmonton, Alberta,  
Canada*

<sup>3)</sup>*Department of Physics, Stockholm University, Stockholm,  
Sweden*

To implement the BB84 decoy-state quantum key distribution (QKD) protocol over a lossy ground-satellite quantum uplink requires a source that has high repetition rate of short laser pulses, long term stability, and no phase correlations between pulses. We present a new type of telecom optical polarization and amplitude modulator, based on a balanced Mach-Zehnder interferometer configuration, coupled to a polarization-preserving sum-frequency generation (SFG) optical setup, generating 532 nm photons with modulated polarization and amplitude states. The weak coherent pulses produced by SFG meet the challenging requirements for long range QKD, featuring a high clock rate of 76 MHz, pico-second pulse width, phase randomization, and 98% polarization visibility for all states. Successful QKD has been demonstrated using this apparatus with full system stability up to 160 minutes and channel losses as high 57 dB<sup>1</sup>. We present the design and simulation of the hardware through the Mueller matrix and Stokes vector relations, together with an experimental implementation working in the telecom wavelength band. We show the utility of the complete system by performing high loss QKD simulations, and confirm that our modulator fulfills the expected performance.

---

<sup>a)</sup>Electronic mail: zyan@iqc.ca

<sup>b)</sup>Electronic mail: thomas.jennewein@uwaterloo.ca

## I. INTRODUCTION

Utilizing ground-to-space quantum communications with satellites to achieve long-distance quantum key distribution (QKD) has been theoretically studied and experimentally proven feasible<sup>2-5</sup>. Ultimately, a global quantum network can be developed by using satellites as trusted nodes. An satellite uplink scheme is appealing because the energy-demanding and relatively complex photon source remains at the ground, easing the requirements on the satellite and granting the ability to use a variety of different sources. Practical QKD apparatuses<sup>6</sup> use either weak coherent pulse (WCP) sources<sup>7-11</sup>, or sources of entangled photon pairs<sup>12-17</sup>. The major challenge of an uplink approach is the additional loss stemming from atmospheric turbulence, leading to low signal compared to the noise of detector dark counts and stray light.

To perform QKD under such challenging conditions, it is desirable to have the source emit single photons within the shortest time window possible. This can be achieved with a mode-locked laser, which intrinsically provides short pulses and a high repetition rate. However such a laser has the inevitable problem of possessing phase correlations between consecutive pulses. This phase correlation violates an assumption of QKD security proofs<sup>9,18</sup>, and is unsuitable as a photon source for QKD without sufficient precaution. To solve this problem, our source produces green photons at 532 nm wavelength by the sum-frequency generation (SFG) process, pumped by a pulsed 810 nm laser and a continuous wave (CW) laser at 1550 nm. The hybrid nature of this design enables us to exploit the repetition rate and pulse width of the mode-locked Ti:Sapphire laser (810 nm), while phase randomization is accomplished with the short coherence length of the telecom laser. Importantly, the photons at 532 nm allow the use of detectors with the highest detection figure of merit<sup>19</sup> available. Additionally, we gain access to fast and stable modulation components designed for the telecom-band around 1550 nm. In this work, we mainly present the telecom intensity and polarization modulator (IPM) to encode quantum keys, as well as the QKD results to verify its performance as one of the building blocks. The SFG nonlinear optical setup is discussed elsewhere<sup>1,20</sup>.

The desired performance for satellite-based QKD previously discussed in, e.g., Refs.<sup>9</sup> and<sup>21</sup>, requires that we consider the following factors when implementing BB84 QKD protocol<sup>22</sup> with the IPM: (1) Polarization encoding in the four non-orthogonal BB84 states<sup>23</sup>.

The main advantage of polarization encoding is that Earth’s atmosphere preserves polarization with high fidelity<sup>24</sup>. (2) Compatible with the SFG setup to produce 532 nm green photons. (3) Compatible with Ti:Sapphire repetition rate, and readily upgradable to several GHz repetition rate.

Previous implementations of polarization modulation for QKD include multiple laser diodes<sup>25</sup>, a single laser diode with multiple optical amplifiers<sup>10</sup>, a single phase modulator with Faraday mirror<sup>26</sup>, as well as a single polarization modulator<sup>9</sup>. The first two approaches<sup>10,25</sup>, due to their using distinct sources of light, face the difficulty of making all output quantum states identical in frequency, bandwidth, and intensity; distinguishing information leads to security loopholes. The latter two methods<sup>9,26</sup> will suffer polarization mode dispersion when two orthogonal modes have to propagate along unsymmetrical optical axes of the same modulator crystal or polarization maintaining fiber, leading to poor polarization states. Long-term thermal stability is also problematic for these implementations, and all exhibit pulse lengths at least two orders of magnitude longer than those obtained with a mode-locked laser.

To avoid the above problems, we present our high speed polarization modulator in the balanced Mach-Zehnder Interferometer (MZI) configuration, including detailed descriptions of its design principles, and analysis of the experimental performance of the modulator. The paper is organized as follows: first we present an overview of the polarization and intensity modulator design, and its role in the entire QKD system; then we discuss the mathematical modelling of the telecom polarization and intensity modulator; finally, we show experimental results and the expected performance of decoy-state QKD based on our design.

## II. ALL-FIBER TELECOM BAND INTENSITY AND POLARIZATION MODULATION SYSTEM: DESIGN, MODELLING AND CHARACTERIZATION

### A. Overview of the QKD source design

Implementing the BB84 protocol with decoy states requires that the output photons have at least two levels of average photon number. In the simplest case, this entails a *signal* state with average photon number  $\mu$  and a *decoy* state with average photon number  $\nu$ . For both

levels, the modulator should output one of four polarization states (horizontal, vertical, diagonal, or anti-diagonal), chosen randomly. For all states, the average photon number per pulse is less than 1 to keep the multi-photon probability low<sup>27</sup>. However, the decoy-state QKD protocol allows for a much larger average photon number (e.g.  $\mu = 0.5$ ) for signal pulses, as compared to WCP QKD protocols not employing decoy states<sup>28</sup>.

Our QKD system is based on the SFG photon scheme as showed in Fig. 1, in order to achieve the required modulation performance, pulse length, and phase randomization at the desired wavelength. The scheme includes a 1550 nm CW laser modulated in amplitude and polarization before being converted to 532 nm through SFG with strong 810 nm pulsed light from the mode-locked Ti:Sapphire laser. An overview of the SFG solution is illustrated in Fig. 1 (a). The SFG green photons' field intensity  $I_3$  for Type-I PPKTP is proportional to the product  $I_1 I_2$  where  $I_1$  and  $I_2$  represent the telecom and 810 nm optical power intensities<sup>29</sup>. The linear dependence of the output intensity of green photons (whose spectrum is shown in Fig. 1 (b)) on the input intensities of both the telecom and 810 nm pumps allows direct modulation of the output light through modulation of only the telecom input. Since we are on at the regime of weak conversion, the spectrum of the generated photons will not be perturbed by the intensities of  $I_1$  and  $I_2$ .

The QKD system has two basic parameters that determine the final key rate and maximum distance: quantum bit error rate (QBER) and sifted key rate. A nonzero QBER is mainly caused by detector dark counts and polarization state visibility<sup>6</sup>. To minimize QBER, by utilizing temporal filtering of detector and background noise, we incorporated thin-silicon SPAD detectors in Bob's receiver. The efficiency of these detectors peaks at a wavelength around 532 nm.

The sifted key rate is determined by the repetition rate of the source, the average photon number  $\mu$ , and channel losses. Pockels cells are capable of switching at such short wavelengths, but they require driving electronics operating at a few kilovolts for a  $\pi$  phase shift ( $V_\pi$ ), preventing such modulators from being operated at the repetition rate of a Ti:Sapphire laser ( $\sim 76$  MHz), let alone approaching GHz rates desirable of high-speed QKD. Instead, our scheme in Fig. 1 allows for using conventional electro-optical (EO) waveguide modulators to match the desired repetition rate.

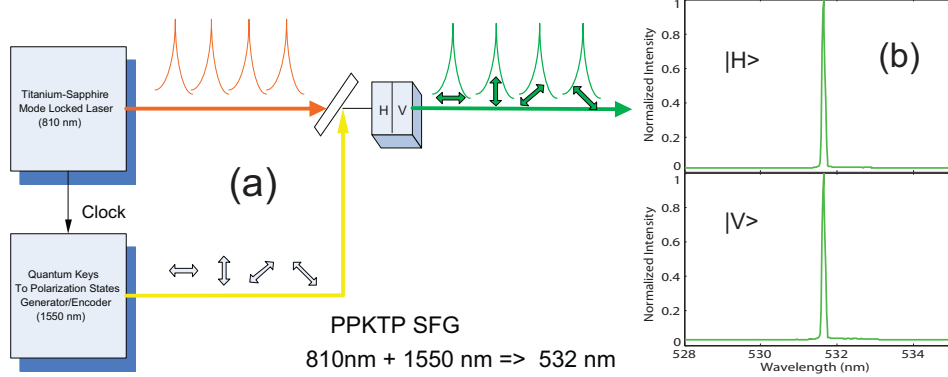


FIG. 1. (a) Generation of QKD polarization states at 532 nm by polarization-preserving SFG through a walk-off compensated PPKTP crystal pair (labeled as H and V, respectively). Light at 810 nm produced by a Ti:Sapphire laser, mode-locked with 76 MHz repetition rate, is combined with 1550 nm light with polarization state engineered by the IPM synchronized to the repetition rate of the Ti:Sapphire laser. The SFG green (532 nm) photons combine properties from both pumping sources, including pulse shape and repetition rate from the Ti:Sapphire laser, and average photon number per pulse and polarization states from the modulated telecom laser. (b) The measured spectrum of green photons produced by our polarization-preserving SFG optical setup. Horizontally and vertically polarized photons have identical spectra.

## B. Overview of the telecom all-fiber modulation system

The telecom modulation system for implementing decoy-state BB84 protocol consists of an intensity modulator followed by a polarization modulator, as realized by two phase modulators in the balanced MZI configuration that is illustrated in Fig. 2 (a). The physical apparatus of this scheme is pictured in Fig. 2 (b). The phase and intensity modulators are customized EO LiNbO<sub>x</sub> modulators from EOSpace, featuring low insertion loss (<2 dB) and external 50 Ω termination of the radio frequency (RF) driving voltage. Their  $V_{\pi}$  is as low as only a few volts, compatible with regular analog-digital mixed signal electronics.

To ensure enough key is being received even when channel loss is high, the system should be capable of modulation at a few hundred MHz. The factors that limit the system clock rate are the finite bandwidth of the modulator drivers, the finite speed of field programmable gate array (FPGA) circuit board, and the interface circuits. The detailed design is displayed in Fig. 2 (a).

The modulator driver circuit is comprised of digital-to-analog interface to bridge FPGA board and the power amplifier that are both adapted to be DC coupled to the RF ports of all modulators. To accomplish wide-band uniformity of the modulation, the driving signal bandwidth ranges from zero to several hundreds of MHz, resulting in reliable switching between any two polarization states. This is particularly important when the RF driving is in the lower frequency regime (e.g. during source testing), because the resulting heat accumulation is detrimental to the stability of polarization states, leading to poor QBER performance.

### C. Modelling of the telecom all-fiber modulation system

We model the action of the modulation system using the Jones matrix approach assuming fully polarized input light and define the following Jones vector for the horizontally polarized state:

$$|H\rangle = \begin{bmatrix} 1 \\ 0 \end{bmatrix}. \quad (1)$$

The system is comprised of an intensity modulator (IM), followed by a polarization beam splitter (PBS) with its fast axis rotated  $45^\circ$  from the input fast axis (represented by a  $\pi/4$  polarization rotation). Both input and output ports of the PBS are coupled to PM fiber. Following this is the balanced MZI, and after which is the polarization beam combiner (PBC) with PM input and single mode (SM) output. The Jones calculus is employed to integrate all of the optical components into a single matrix  $[J]$ <sup>30</sup>

$$[J] = \left[ \text{QWP} \left( -\frac{\pi}{4} \right) \right] [\text{PBC}] [\text{MZI}] [\text{PBS}] \left[ \text{Ro} \left( \frac{\pi}{4} + \delta \right) \right]. \quad (2)$$

The last  $[\text{QWP} (-\frac{\pi}{4})]$  is used to rotate from modulation in the circular-diagonal polarization plane to the linear polarization plane, and is performed by FPC.2 in the apparatus.

We consider the intensity modulator separately as it acts globally on the total output intensity independent of polarization. Its mathematical model, as usually defined, is  $\text{IM}(V_0) = \frac{1}{2} \left\{ 1 + b \cos \left( \frac{V_0}{V_\pi} \pi + \Phi_1 \right) \right\}$  where  $0 \leq b \leq 1$  is modulation depth and  $\Phi_1$  is the zero voltage phase, adjustable by applying an external DC bias. The applied voltage is  $V_0$  and the voltage parameter  $V_\pi$  is defined in Ref.<sup>31</sup> as:  $V_\pi = \frac{\lambda}{n_0^3 r_{ij}} \frac{d}{\gamma L}$  in which  $r_{ij}$  is the linear electro-optical tensor element,  $n_0$  is the zero voltage refractive index,  $\gamma$  is the optical confinement coefficient,  $L$  is the length of waveguide, and  $d$  is the gap distance of transmission line

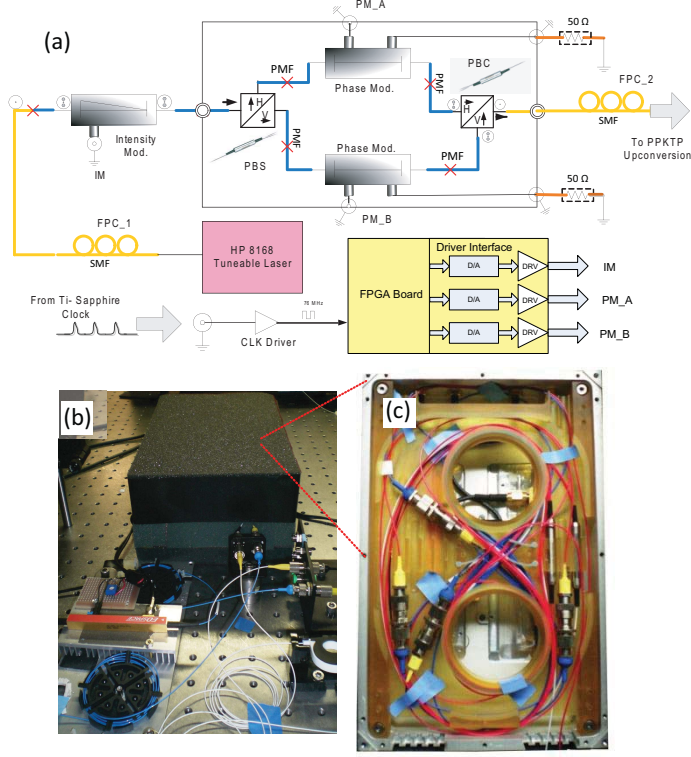


FIG. 2. (a) Diagram of the intensity and polarization modulator. Signal and decoy states are realized by the intensity modulator, and polarization modulation by the balanced MZI, where each arm contains an EO phase modulator. The input and output to the modulator are a polarization beam splitter and a polarization beam combiner, respectively. The FPGA logic and digital & analog mixed signal board provide the encoding and driving voltages to the phase modulators and intensity modulator. The FPGA board is interfaced to three independent channels of fast digital to analog converter (D/A) circuits. The RF driving amplifier (DRV) are DC coupled to three ports of EO modulators. Two paddle-wheel fiber polarization controllers (FPCs) are used to adjust the input and output polarization states. Thick yellow lines (color) illustrate standard single mode fiber (SMF); thick blue lines (color) represent polarization-maintaining fiber (PMF); each red cross (color) indicates narrow key FC/PC connectors, enabling high-precision polarization coupling between two connecting optical fibers. The FPGA system clock is externally obtained from the PIN diode pulses of a mode-locked Ti-Sapphire laser. Those pulses are amplified via a pulse shaping circuit to generate 76 MHz TTL clock signal. (b) Photo of modulators including intensity (external PM fiber coupled) and phase modulators, as well as the polarization beam splitters and combiners (sealed in a thermally insulating box). (c) The core of this polarization modulator, comprised of a pair of phase modulators at the lower level, and one each of polarization beam splitter and combiner.

that is excited by the modulator electrode input voltage. For the intensity modulator, the theoretical curve with  $b = 1$  and  $V_\pi = 4.0$  V is the best fit for the experimental verification, and we measured an extinction ratio of our apparatus reaching 30 dB.

In coupling from the IM to the MZI, the actual PBS component has a small rotation offset  $\delta$  from the desired  $45^\circ$ , resulting in unequal splitting of the input beam. Thus the real device can be modelled as

$$\text{Ro}\left(\frac{\pi}{4} + \delta\right) = \frac{1}{\sqrt{2}} \begin{bmatrix} \cos \delta - \sin \delta & \cos \delta + \sin \delta \\ -\cos \delta - \sin \delta & \cos \delta - \sin \delta \end{bmatrix}. \quad (3)$$

In the MZI polarization modulator, the relative phase delay between the two arms is controlled by high frequency or DC voltages on each modulator of  $V_1$  and  $V_2$  respectively, in the push-and-pull mode. The effect of the PBS and PBC are included implicitly in the Jones calculus, as the matrix for the MZI is diagonal:

$$\text{MZI}(V_1, V_2) = \begin{bmatrix} \exp\left[j\left(\frac{V_1}{V_\pi}\pi + \Phi_0\right)\right] & 0 \\ 0 & \exp\left[j\left(\frac{V_2}{V_\pi}\pi\right)\right] \end{bmatrix}, \quad (4)$$

where  $V_\pi$  is the  $\pi$  phase shift voltage for each phase modulator, and  $\Phi_0$  is the zero-voltage phase between two modulators arising from the length imbalance of two arms, denoted  $\Delta L$ . The value of  $\Delta L$  introduces temperature-caused instabilities into the system and plays an important role in determining the operating wavelength and voltages of the MZI as seen below. To find its value, we perform a wavelength scan over a range of more than 2 nm around 1550 nm. When a linear polarizer and a quarter waveplate are placed after the PBC, the transmitted intensity  $I_{tr}$  exhibits an oscillation:

$$I_{tr} = \frac{1}{2}I_0(1 + \cos(2\vartheta)\cos\Phi_0). \quad (5)$$

where  $\vartheta$  is the angle of polarizer with respect to the optical axis of MZI,  $I_0$  is the input intensity of MZI.  $\Phi_0$  is a function of wavelength  $\lambda$  as  $\Phi_0(\lambda) = n_1\frac{2\pi}{\lambda}\Delta L$ . Here  $n_1$  is the effective refractive index in the optical fiber, taken as constant over the wavelengths of interest; for wider wavelength range, dispersion in the fiber must be taken into account. If we use wave number  $m = \frac{1}{\lambda}$ , then  $\Phi_0$  becomes a linear function of  $m$  as  $2n_1\pi m\Delta L$ . Eq. 5 is plotted in Fig. 3 versus  $m$  and compared with the experimental results. Based on the data in Fig. 3, we compute  $\Delta L = 6.0 \times 10^{-3}$  m. Since  $n_1$  is also a function of temperature and wavelength, exactly determining the optimal  $\Phi_0$  requires further fine tuning the input

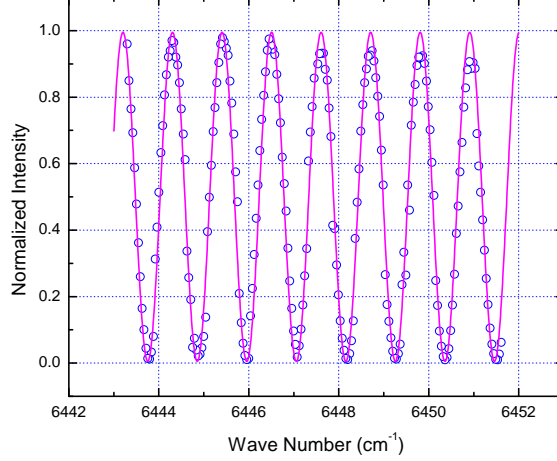


FIG. 3. The measured intensity oscillation after a linear polarizer and a quarter wave plate when the input wavelength of our MZI modulator is varied. The solid line represents simulation data; hollow circles are the measured results.

wavelength. In order to study polarization intensities as Stokes vector elements, we need to convert the Jones calculus into a Mueller calculus. The Mueller matrix for a given Jones matrix can be<sup>30</sup> converted using  $M = A \cdot (J \otimes J^*) \cdot A^{-1}$  with

$$A = \begin{bmatrix} 1 & 0 & 0 & 1 \\ 1 & 0 & 0 & -1 \\ 0 & 1 & 1 & 0 \\ 0 & j & -j & 0 \end{bmatrix}.$$

By transforming the matrix  $[J]$  in Eq. 2, we find the Mueller matrix corresponding to our polarization modulator:

$$M_O = \begin{bmatrix} 1 & 0 & 0 & 0 \\ 0 & \cos(\Theta) \cos(2\delta) & \cos(\Theta) \sin(2\delta) & -\sin(\Theta) \\ 0 & \sin(\Theta) \cos(2\delta) & \sin(\Theta) \sin(2\delta) & \cos(\Theta) \\ 0 & \sin(2\delta) & -\cos(2\delta) & 0 \end{bmatrix}, \quad (6)$$

where  $\Theta = \frac{V_1 - V_2}{V_\pi} \pi + \Phi_0$  is the voltage modulation angle mediated by  $V_1$  and  $V_2$ , which are the phase modulator voltages, and  $\Phi_0$  has been discussed by Eq. (5);  $\delta$  is the angular deviation from perfect  $45^\circ$  input polarization. Now we take the input as linearly polarized as in Eq. (1), such that the input Stokes vector is  $S = (1 \ 1 \ 0 \ 0)^T$ . The output of the

polarization modulator (multiplication by  $M_O$  of Eq. (6)) is then

$$\begin{bmatrix} S_0 \\ S_1 \\ S_2 \\ S_3 \end{bmatrix} = \begin{bmatrix} 1 \\ \cos\left(\frac{V_1-V_2}{V_\pi}\pi + \Phi_0\right)\cos(2\delta) \\ \sin\left(\frac{V_1-V_2}{V_\pi}\pi + \Phi_0\right)\cos(2\delta) \\ \sin(2\delta) \end{bmatrix}. \quad (7)$$

Eq. (7) indicates the two degrees of freedom that are outside direct control by the phase modulator voltages: the intensity imbalance of the arms modelled by deviation angle  $\delta$ , and the initial phase angle  $\Phi_0$  which stems from the optical path difference between the MZI arms. The non-ideal splitting angle  $\delta$  can usually be eliminated by carefully adjusting fiber polarization controller FPC\_1 in Fig. 2. To set the initial phase  $\Phi_0$  to the optimal value ( $\pi/4$ ) where minimal driving voltages are needed, we varied the wavelength of the telecom laser (HP 8168 is illustrated in Fig. 2) based on Eq. (5). After these two adjustments, we have the output polarization states

$$\begin{bmatrix} S_0 \\ S_1 \\ S_2 \\ S_3 \end{bmatrix} = \begin{bmatrix} 1 \\ \sin\left(\frac{V_1-V_2}{V_\pi}\pi + \frac{\pi}{4}\right) \\ \cos\left(\frac{V_1-V_2}{V_\pi}\pi + \frac{\pi}{4}\right) \\ 0 \end{bmatrix}. \quad (8)$$

Thus, using our modulator, it is possible to output any polarization on the equator of the Poincaré sphere by controlling the phase voltages  $V_1$  and  $V_2$ . Simulation results are shown in Fig. 4 (a). To confirm the accuracy of the simulation, we have performed polarization measurements with an Agilent N7788B optical component analyzer; the results of this are shown in Fig. 4 (b). To control the phase modulators for these measurements, we supply two triangular waves with a  $\pi$  phase difference to the RF ports of the modulators.

The states of interest for BB84 and corresponding ideal control voltages are listed in Table I. Driving voltages are minimized when  $\Phi_0 = \frac{\pi}{4}$  to reduce power dissipation in the driver. The driving voltages are chosen such that the voltage settings are symmetric around zero volts, resulting in zero DC bias voltage. The maximum sampling speed of the polarization analyzer we used is 0.1 MHz, much less than the 76 MHz system clock rate. Thus, to characterize the polarization states at higher speed, we developed a new method which we describe below.

TABLE I. The driving voltage settings of two arms and corresponding output polarization states. The value of voltages labeled in the right hand figure is  $V_1 - V_2$ .

$V_1$	$V_2$	State
$\frac{V_\pi}{8}$	$-\frac{V_\pi}{8}$	H
$-\frac{V_\pi}{8}$	$\frac{V_\pi}{8}$	D
$-\frac{3V_\pi}{8}$	$\frac{3V_\pi}{8}$	V
$\frac{3V_\pi}{8}$	$-\frac{3V_\pi}{8}$	A

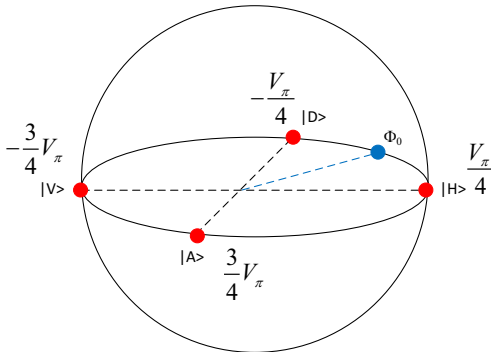
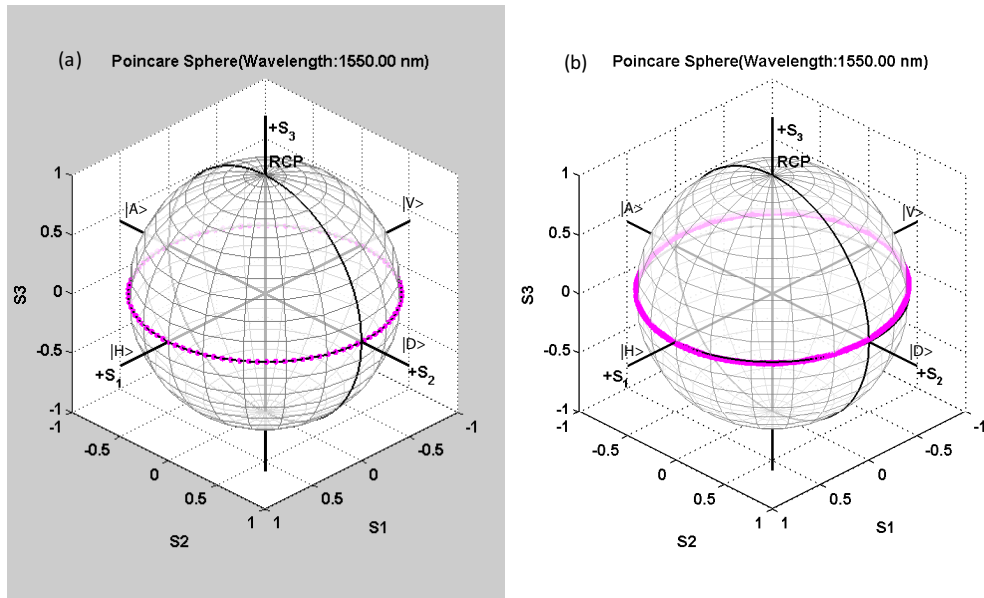



FIG. 4. Poincaré sphere traces of the light passing through the polarization modulator, due to a triangular shaped voltage. (a) Simulation results; (b) experimental measurements. (a) and (b) are determined after the polarization controller FPC\_2 and include the unitary transformation  $\text{QWP}(\frac{\pi}{4})$  to bring the modulation to the equator of the Poincaré sphere. The polarization states are measured by an Agilent N7788B Optical Component Analyzer, and the Polarization Navigator software package.

#### D. Polarization state characterization

We wish to know the exact output polarization state described by Eq. (7) at full modulation speed. It is impossible to do a direct characterization of the Stokes vectors using

standard polarimeters due to the high repetition rate of the modulator. Here we use a quarter waveplate (QWP) followed by a linear polarizer with a repeated modulation sequence that allows us to extract the Stokes parameters of each state in the sequence. The intensity  $S_j^\pm$  after the QWP and polarizer is calculated in Ref.<sup>32</sup>

$$S_j^\pm = \frac{1}{2} \left\{ S_0 + (S_1 \cos 2\beta_j + S_2 \sin 2\beta_j) \cos 2(\alpha_j - \beta_j) \right. \\ \left. + [(S_2 \cos 2\beta_j - S_1 \sin 2\beta_j) \cos \Delta + S_3 \sin \Delta] \right. \\ \left. \times \sin 2(\alpha_j - \beta_j) \right\}, \quad (9)$$

where  $\alpha_j$  is the angle of the linear polarizer's transmission axis and  $\beta_j$  is the angle of the fast axis of the QWP—in our experiment, angles  $\alpha_j$  and  $\beta_j$  are both with respect to horizontal. The retarder phase delay  $\Delta$  is  $\pi/2$  for a QWP, however in real devices there exists non-trivial deviations to this ideal value. In our setup, we use a QWP from Thorlabs and find 7% offset from  $\frac{\pi}{2}$ .

At least three measurements with the settings defined in Table II were performed to obtain three components ( $S_1^+$ ,  $S_2^+$ , and  $S_3^+$ ) taken at 2 MHz modulation speed. The results are displayed in Fig. 5 (a). This characterization scheme utilized an optical detector (Thorlabs PDA10CF) which had a bandwidth of 150 MHz.

In Fig. 5 (a), there is a time displacement of around 100 ns between the differential voltage  $V_1 - V_2$  and polarization states due to the delays between the optical and electrical signals. The spike overshoot is due to the finite transition time across multiple polarization states, when the differential driving voltage has the largest step. The transition ring ripples after the spike is caused by the limited response time of the optical PIN diode, but the actual polarization states should not be affected. Moreover, since the upconversion SFG process only occurs in a time overlap (less than 1 ns) when both telecom and 810 nm photons arrive, the polarization states of telecom photons within a few percentage of each repetition cycle are responsible for the green photon states. We are able to completely avoid the transition spike by moving the overlap time to the end of each cycle.

In the subsequent simulation, we have modeled the entire IPM system as well as the polarization characterization optics. The imperfection of QWP was also take this into account. The degree of polarization (DOP) was experimentally found to be over 99%, hence  $S_0$  can be determined by the averaged maximum intensity. We then use the relations  $S_1 = 2S_1^+ - S_0$ ,  $S_2 = 2S_2^+ - S_0$ , and  $S_3 = 2S_3^+ - S_0$  to determine the exact polarization states in H/V, D/A,

TABLE II. Measurement settings for polarization state characterization

$S_j^\pm$	Linear Polarizer ( $\alpha_j$ )	Quarter-Wave Plate ( $\beta_j$ )
$S_1^+$	$0^\circ$	$0^\circ$
$S_2^+$	$45^\circ$	$45^\circ$
$S_3^+$	$45^\circ$	$0^\circ$

and L/R bases, respectively, for each modulation setting ( $V_1$  and  $V_2$ ). The simulation results compared with the extracted Stokes vector elements  $S_1$ ,  $S_2$  and  $S_3$  (in hollow square) are displayed in Fig. 5 (b). For each extraction point, the  $x$  error bar indicates the length of time (125 ns) to average the polarization states; the  $y$  error bar indicates the uncertainty of each extraction.

### E. Temperature Stability of the Modulator

The temperature stability of the polarization state plays a critical role for long-term operation of this device. To measure the performance of a given polarization state against the variation of ambient temperature, we use a constant optical power and wavelength at the input port of our polarization controller, and measure the output power of four polarization components by our in-house-developed polarimetry method described in the previous section.

Fig. 6 shows the measurement results for H/V and D/A components. The temperature is maintained by a Thorlabs TC-200 controller. In this measurement, no voltage is applied to either the phase or intensity modulators, but the initial phase  $\Phi_0$  in the MZI becomes a function of temperature. By carefully eliminating the L/R components, the output polarization state sweeps across the equator of the Poincaré sphere (provided that the temperature variation is big enough) as indicated by Fig. 6.

However, at higher temperature settings when the temperature setting is  $> 30^\circ\text{C}$ , the temperature actuator (heater) cycles through on and off states more frequently, resulting in strong fluctuations and poor visibility. This is due to the simple point contact heater used—it takes some time for the temperature of the arms of the MZI to stabilize, and more importantly two arms are not heated up equally leading to adversely increasing the imbalance of MZI. A two-stage heater would be desirable for achieving better long term temperature stabilization.

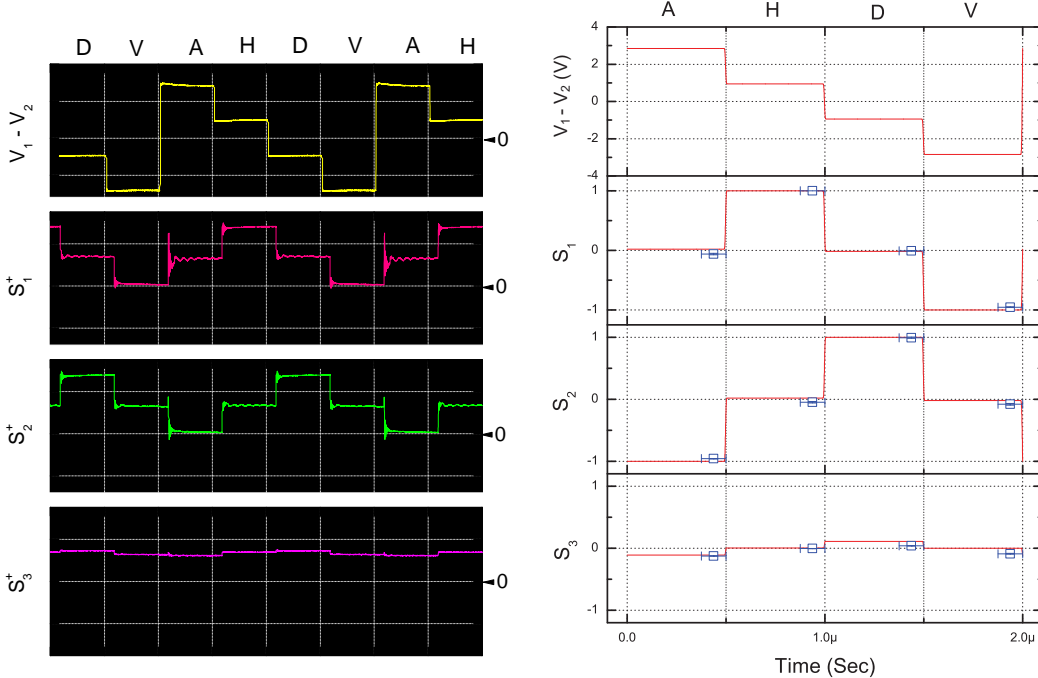


FIG. 5. (a) The oscilloscope traces to measure Stokes vector including differential voltage  $V_1 - V_2$  between two phase modulators located at two arms of MZI; three measurements for  $S_1^+$ ,  $S_2^+$  and  $S_3^+$  at a wavelength of 1550.5 nm. All of the raw signal traces were collected by an Agilent DSO8104A Infiniium Oscilloscope. Each horizontal division was set to be 500 ns in the plot; the differential voltage plot had 2 volts per division for its vertical trace; while the rest three plots had 100 mV per division. (b) The simulation results for wavelength  $\lambda = 1550.5$  nm, with measured three Stokes vector elements normalized to  $S_0$  (in blue hollow squares with error bars). The simulation includes the imperfect retardance (7%) of the QWP; the time delay between differential voltage to the polarization states has not been taken into account.

### III. EXPERIMENTAL RESULTS OF INTENSITY AND POLARIZATION MODULATOR IMPLEMENTING BB84 PROTOCOL WITH DECOY STATES

#### A. Theory of BB84 protocol with decoy states

WCP QKD, attractive for its simple designs and high rates, is subject to the photon number splitting attack<sup>33</sup> due to the nonzero probability of producing multiple photons in a single laser pulse. To securely achieve any reasonable transmission distance requires the in-

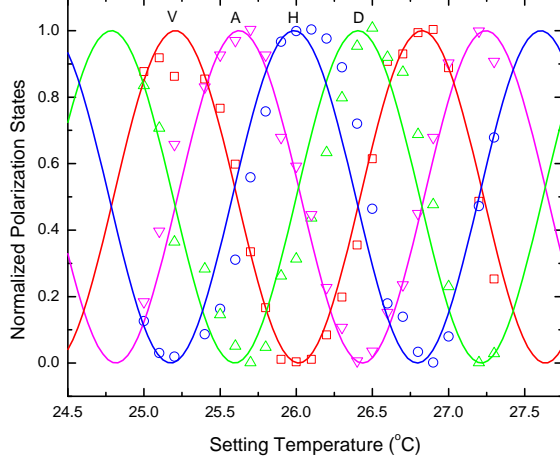


FIG. 6. The measured power of four polarization states as temperature varies. The setting of temperature is monitored and maintained by a Thorlabs TC-200 temperature controller driving a point contact heater in the enclosure of the MZI polarization controller.

clusion of decoy states, i.e. pulses with differing intensities used to bound the eavesdropper's information from multi-photon events<sup>28,34</sup>. We implement a polarization-encoded protocol with vacuum+weak decoy states<sup>27</sup>. To calculate the final secure key rate, we must estimate the single-photon gain and error rate. We calculate a lower bound of single photon gain  $Q_1^L$  from Ref.<sup>27</sup> as

$$Q_1^L = \frac{\mu^2 e^{-\mu}}{\mu\nu - \nu^2} \left( Q_\nu e^\nu - Q_\mu e^\mu \frac{\nu^2}{\mu^2} - \frac{\mu^2 - \nu^2}{\mu^2} Y_0 \right), \quad (10)$$

where  $\mu$  is the average photon number for signal states and  $\nu$  for decoy states, and  $Q_{\mu/\nu}$  are the gains for these two states.  $Y_0$ , the vacuum yield, is determined by the detector dark counts and background noise, and was measured between non-vacuum pulses. Similarly, the upper bound on the error rate,  $\varepsilon_1^U$ , of single photon states is

$$\varepsilon_1^U = \frac{E_\nu Q_\nu e^\nu - e_0 Y_0}{\nu Q_1^L} \mu e^{-\mu}, \quad (11)$$

where  $E_\nu$  is the total error rate for decoy states, and  $e_0 = 0.5$  is the vacuum error rate. After evaluation of the parameters in Eqs. (10) and (11), we can find the lower bound of the secret key rate per pulse,  $R$ :

$$R = q L_{\mu(\nu')} \left\{ -Q_\mu f(\text{QBER}) H_2(\text{QBER}) + Q_1^L [1 - H_2(\varepsilon_1^U)] \right\}. \quad (12)$$

where  $q = 1/2$  is the basis reconciliation factor,  $L_{\mu\nu} = N_\mu / (N_\mu + N_\nu)$  is the ratio of signal pulses to the total pulses, and QBER is the total quantum bit error rate for signal pulses. For

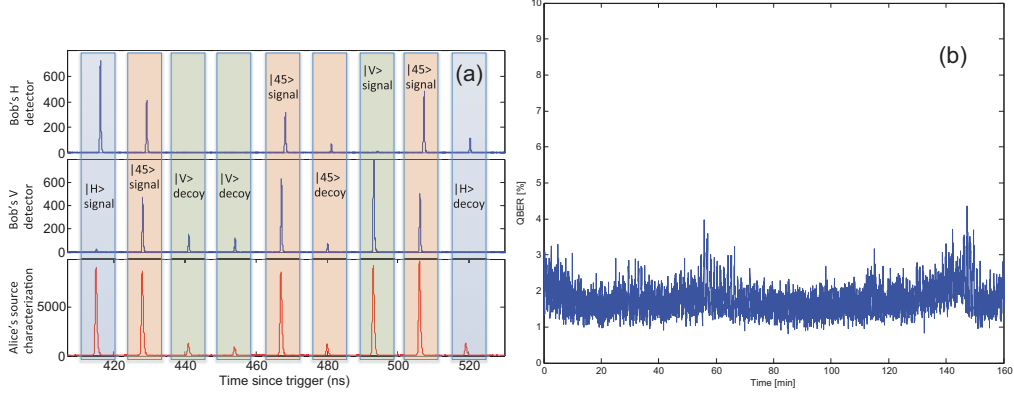


FIG. 7. (a) Experimental measurements for the decoy+signal QKD states accumulated in the histogram format (see<sup>20</sup> in which Bob’s detector was fixed to an H/V basis measurement.).  $|45\rangle$  indicates either a D or A polarization state which is not resolved by our two-detector receiver in this basis. (b) Stability measurement of the overall QKD system-wide QBER over consecutive 160 minutes at 25 dB total loss, showing the averaged QBER at  $1.8 \pm 0.9\%$ . The system clock rate is 76 MHz triggered from the Ti-Sapphire mode-locked laser.

the calculations here, a constant error correction efficiency  $f(\text{QBER})$  of 1.22 was assumed.

## B. Experimental Demonstration of High Loss QKD System

Our complete system exhibits high performance: when the 810 nm laser is not mode-locked (i.e. continuous wave), the output photons at 532 nm have a fidelity  $>99\%$  with the desired polarization states. Upon mode-locking and fast modulation, we find that our system fidelity including all losses and error sources is maintained at  $>98\%$  in the H/V polarization basis, and  $>95\%$  in the D/A basis. The modulation achieves accurate average photon number per pulse for both decoy and signal states, sufficient to perform successful QKD. Fig. 7 (a) demonstrates the measured photon output for signal and decoy states with various polarizations. We additionally implemented an automated polarization alignment procedure in the quantum receiver to keep high fidelity for all four states, the details of which will be published elsewhere. Fig. 7 (b) illustrates a QBER stability measurement over more than 160 minutes with ambient temperature fluctuation  $<0.5^\circ\text{C}$ . The QBER shows an average value of  $1.8 \pm 0.9\%$ , a very small variation. Our simulations of ground-to-space quantum channels show that the overall QBER of our system is sufficient for a satellite

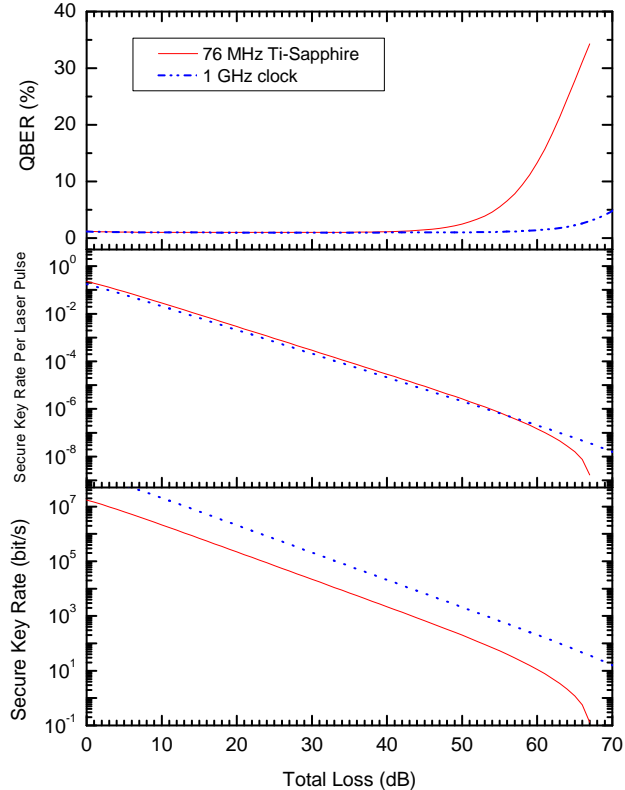


FIG. 8. The projected performance of our decoy state BB84 QKD system. We show the simulation results of QBER, secure key rate probability per pumping laser pulse, and the final key rate under total channel loss. We assume two pumping laser rates: the currently used Ti-Sapphire laser pumping rate of 76 MHz (solid red line), and the projected 1 GHz clock rate (dashed blue line).

uplink<sup>35</sup>.

Finally, we calculate the secure key rate based on Eq. (12). The result is shown in Fig. 8, in which the detector efficiency is 60% and the dark count rate is 50 counts/s. The intrinsic QBER is 1%, which accounts for the optical misalignments in the telecom modulator, SFG source, and receiver. In practice, stray light will lead to slightly higher measured QBER than the simulated value under the same channel loss. The signal and decoy states are 0.6 and 0.2 photons per pulse respectively. QKD beyond 60 dB total loss is possible with this system.

## IV. CONCLUSION AND OUTLOOK

We have presented our design and implementation of a Mach-Zehnder configuration, all-fiber, intensity and polarization modulator. This design features very high switching speed and high polarization visibility. Our modulator serves as a secret key encoder which can easily be upgraded to GHz speeds owing to the rich choice of photonic devices for telecom wavelengths. We used this modulator and the SFG process to produce 532 nm green photons at a repetition rate near one hundred MHz, which is the highest speed for this operating wavelength demonstrated so far. The green photons show excellent polarization state fidelity, and are compatible with the highest figure of merit single photon detectors commercially available.

The quantum optical simulations in Fig. 8 show QKD is possible over channels beyond 60 dB of loss. Additionally, we measured the raw key rates, average photon numbers for signal and decoy states, and quantum bit error rates with high channel losses. The performance fulfills the design goals of the telecom modulator and agrees with our quantum optics simulation results. Assuming an average loss of 45 dB for a LEO satellite passage, the final secure key rate is 155 bit/s.

If we employ a 1 GHz repetition rate pumping laser, the operating clock rate of our telecom modulator can be readily boosted accordingly, thanks to the technological advancement of FPGA<sup>36</sup> and RF power electronics<sup>37</sup>. Assuming this increased speed, the QBER, secure key rate per pulse and per second are displayed in Fig. 8 as dashed lines. At the same average LEO satellite channel loss, the secure key rate will be  $\sim 2300$  bit/s, an increase of more than an order of magnitude, and better than the repetition rate increase factor owing to an improved signal-to-noise ratio. Consequently, we present our system that is able to overcome the high channel loss that plagues proposals for a satellite uplink QKD system with our current setup. Our experimental results verify the feasibility of using such a source in a near term satellite mission. Using higher speed modulation such as 1 GHz rate, it is possible to achieve higher secret key rate and to withstand higher channel losses.

## V. ACKNOWLEDGMENT

This work is supported by Natural Sciences and Engineering Research Council of Canada (NSERC), Canadian Space Agency (CSA), COM DEV International Ltd., Canada Foundation for Innovation (CFI), Industry Canada, and Canadian Institute for Advanced Research (CIFAR). We would like to thank Agilent Technologies Inc., and General Photonics Inc. for providing us optical measurement instruments.

## REFERENCES

- <sup>1</sup>E. Meyer-Scott, Z. Yan, A. MacDonald, J.-P. Bourgoïn, H. Hübel, and T. Jennewein, *Phys. Rev. A* **84**, 062326 (2011).
- <sup>2</sup>J. G. Rarity, P. R. Tapster, P. M. Gorman, and P. Knight, *New Journal of Physics* **4**, 82 (2002).
- <sup>3</sup>E.-L. Miao, Z.-F. Han, T. Zhang, and G.-C. Guo, *Physics Letters A* **361**, 29 (2007).
- <sup>4</sup>P. Villoresi, T. Jennewein, F. Tamburini, M. Aspelmeyer, C. Bonato, R. Ursin, C. Pernechele, V. Luceri, G. Bianco, A. Zeilinger, and C. Barbieri, *New Journal of Physics* **10**, 033038 (12pp) (2008).
- <sup>5</sup>C. Bonato, A. Tomaello, V. D. Deppo, G. Naletto, and P. Villoresi, *New Journal of Physics* **11**, 045017 (25pp) (2009).
- <sup>6</sup>N. Gisin, G. Ribordy, W. Tittel, and H. Zbinden, *Rev. Mod. Phys.* **74**, 145 (2002).
- <sup>7</sup>A. R. Dixon, Z. L. Yuan, J. F. Dynes, A. W. Sharpe, and A. J. Shields, *Opt. Express* **16**, 18790 (2008).
- <sup>8</sup>A. R. Dixon, Z. L. Yuan, J. F. Dynes, A. W. Sharpe, and A. J. Shields, *Applied Physics Letters* **96**, 161102 (2010).
- <sup>9</sup>M. Jofre, A. Gardelein, G. Anzolin, G. Molina-Terriza, J. P. Torres, M. W. Mitchell, and V. Pruneri, *J. Lightwave Technol.* **28**, 2572 (2010).
- <sup>10</sup>M. Jofre, A. Gardelein, G. Anzolin, W. Amaya, J. Capmany, R. Ursin, L. Penate, D. Lopez, J. L. S. Juan, J. A. Carrasco, F. Garcia, F. J. Torcal-Milla, L. M. Sanchez-Brea, E. Bernabeu, J. M. Perdigues, T. Jennewein, J. P. Torres, M. W. Mitchell, and V. Pruneri, *Opt. Express* **19**, 3825 (2011).

- <sup>11</sup>D. Stucki, N. Walenta, F. Vannel, R. T. Thew, N. Gisin, H. Zbinden, S. Gray, C. R. Towery, and S. Ten, *New Journal of Physics* **11**, 075003 (2009).
- <sup>12</sup>T. Jennewein, C. Simon, G. Weihs, H. Weinfurter, and A. Zeilinger, *Phys. Rev. Lett.* **84**, 4729 (2000).
- <sup>13</sup>S. Tanzilli, W. Tittel, H. De Riedmatten, H. Zbinden, P. Baldi, M. DeMicheli, D. Ostrowsky, and N. Gisin, *The European Physical Journal D - Atomic, Molecular, Optical and Plasma Physics* **18**, 155 (2002).
- <sup>14</sup>E. Meyer-Scott, H. Hubel, A. Fedrizzi, C. Erven, G. Weihs, and T. Jennewein, *Applied Physics Letters* **97**, 031117 (2010).
- <sup>15</sup>X. Ma, C.-H. F. Fung, and H.-K. Lo, *Physical Review A* **76**, 012307 (2007).
- <sup>16</sup>C. Erven, X. Ma, R. Laflamme, and G. Weihs, *New Journal of Physics* **11**, 045025 (15pp) (2009).
- <sup>17</sup>M. Aspelmeyer, T. Jennewein, M. Pfennigbauer, W. R. Leeb, and A. Zeilinger, *IEEE Journal of Selected Topics in Quantum Electronics* **9**, 1541 (Nov.-Dec. 2003).
- <sup>18</sup>D. Gottesman, H.-K. Lo, N. Lütkenhaus, and J. Preskill, *Quantum Information and Computation* **4**, 325 (2004).
- <sup>19</sup>R. H. Hadfield, *Nat Photon* **3**, 696 (2009).
- <sup>20</sup>E. Meyer-Scott, *Experimental quantum communication in demanding regimes*, Master's thesis, University of Waterloo (2011).
- <sup>21</sup>F. Dios, J. A. Rubio, A. Rodríguez, and A. Comerón, *Appl. Opt.* **43**, 3866 (2004).
- <sup>22</sup>C. H. Bennett and G. Brassard, *International Conference on Computers, Systems & Signal Processing* (1984).
- <sup>23</sup>X. Liu, C. Liao, J. Mi, J. Wang, and S. Liu, *Physics Letters A* **373**, 54 (2008).
- <sup>24</sup>M. Toyoshima, H. Takenaka, Y. Shoji, Y. Takayama, Y. Koyama, and H. Kunimori, *Opt. Express* **17**, 22333 (2009).
- <sup>25</sup>Y. Liu, T.-Y. Chen, J. Wang, W.-Q. Cai, X. Wan, L.-K. Chen, J.-H. Wang, S.-B. Liu, H. Liang, L. Yang, C.-Z. Peng, K. Chen, Z.-B. Chen, and J.-W. Pan, *Opt. Express* **18**, 8587 (2010).
- <sup>26</sup>I. Lucio-Martinez, P. Chan, X. Mo, S. Hosier, and W. Tittel, *New Journal of Physics* **11**, 095001 (2009).
- <sup>27</sup>X. Ma, B. Qi, Y. Zhao, and H.-K. Lo, *Phys. Rev. A* **72**, 012326 (2005).
- <sup>28</sup>H.-K. Lo, X. Ma, and K. Chen, *Phys. Rev. Lett.* **94**, 230504 (2005).

- <sup>29</sup>R. W. Boyd, “Nonlinear optics,” (London : Academic Press, 2003) Chap. 3, 2nd ed.
- <sup>30</sup>H. Fujiwara, *Spectroscopic Ellipsometry: Principles and Applications* (Hoboken: John Wiley & Sons, Ltd, 2007, Appendix 4).
- <sup>31</sup>G. Li and P. Yu, Lightwave Technology, Journal of **21**, 2010 (2003).
- <sup>32</sup>H. G. Berry, G. Gabrielse, and A. E. Livingston, Appl. Opt. **16**, 3200 (1977).
- <sup>33</sup>G. Brassard, N. Lütkenhaus, T. Mor, and B. C. Sanders, Phys. Rev. Lett. **85**, 1330 (2000).
- <sup>34</sup>W.-Y. Hwang, Phys. Rev. Lett. **91**, 057901 (2003).
- <sup>35</sup>J. Bourgoin, E. Meyer-Scott, B. L. Higgins, B. Helou, C. Erven, H. Huebel, B. Kumar, D. Hudson, I. D’Souza, R. Girard, N. Lütkenhaus, R. Laflamme, and T. Jennewein, In Preparation.
- <sup>36</sup><http://www.xilinx.com/products/silicon-devices/fpga/index.htm/> (), [Online; accessed 03-August-2012].
- <sup>37</sup><https://www.hittite.com/> (), [Online; accessed 03-August-2012].